Journal of Computer Science

Original Research Paper

Whale Optimized Deep Generative Adversarial Network Based Alzheimer's Stages Detection Using 3D MRI Brain Neuroimaging

[1,2]R. Sampath and [3]M. Baskar

[1]Department of Computer Science and Engineering, School of Computing, College of Engineering and Technology, SRM Institute of Science and Technology, Kattankulathur, Chengalpattu, Tamil Nādu, 603203, India
[2]Department of Information Technology, Sri Sairam Institute of Technology Chennai, Tamil Nadu, 600044, India
[3]Department of Computing Technologies, School of Computing, College of Engineering and Technology, SRM Institute of Science and Technology, Kattankulathur, Chengalpattu, Tamil Nādu, 603203, India

Article history
Received: 24-04-2023
Revised: 06-06-2023
Accepted: 06-07-2023

Corresponding Author:
M. Baskar
Department of Computing Technologies, School of Computing, College of Engineering and Technology, SRM Institute of Science and Technology, Kattankulathur, Chengalpattu, Tamil Nādu, 603203, India
Email: baashkarinfo@gmail.com

Abstract: Alzheimer's Disease (AD), a common, chronic neurodegenerative condition, is characterized by the loss of neurons and synapses in the cerebral cortex and specific subcortical regions. According to claims from a recent study, AD has a 20% misdiagnosis rate. Therefore, it is essential to create a useful tool to recognize the stages of AD with a lower prediction error rate to reduce misdiagnosis. Hence proposed a model called Whale-Optimized Deep Generative Adversarial Network (WODGAN). A generator plus a discriminator make up the model. The discriminator trains the model using real images; The generator creates synthetic images using noise and random selection. The discriminator goes through some processes to improve image quality, including Adaptive Histogram Equalization (AHE) and Adaptive Filtering (AF) approaches. Fuzzy feature extraction techniques are used to accurately segregate biomarker regions from brain MRI scans depending on AD pathology. The model uses Hilbert-Schmidt Independence Criterion Lasso (HSICL) to discover optimized biomarker features to combat overfitting. Before training, the discriminator can tell actual photos from artificial ones. The Whale Optimizer (WO) is used during training to improve network efficiency and lower prediction errors. The numerical results show a high accuracy of 99.93% in AD stage recognition.

Keywords: Alzheimer's Disease, 3D MRI Brain Neuroimaging, Biomarker Feature, Feature Extraction, Deep Generative Adversarial Networks, Fuzzy Neutrosophic Logic Region Growing, Whale Optimize, Image Enhancement

Introduction

Alzheimer's is a neurodegenerative disorder (Brazaca *et al*., 2020) characterized by progressive and irreversible cognitive decline. The causes of AD are poorly understood: About 70% of the risk is present at birth in patients with many genes frequently involved. Other general risk factors are a history of head injury, depression, and hypertension. As of the 2020 report, approximately 50 million people worldwide suffer from various AD stages. Clinical stages of AD are Cognitive Normal (CN) (Nawaz *et al*., 2021), Significant Memory Concern (SMC) (Kazemi and Houghton, 2018), Mild Cognitive Impairment (MCI) (Leandrou *et al*., 2018) and AD (Shi *et al*., 2017a). While AD is at the normal cognitive stage, the patient shows no signs of the disease, including depression, MCI, or dementia. With cognitive variation indices and a clinical dementia grade of 0, SMC indicates that the patient is self-reporting significant memory apprehension. Patients' scores are now within the normal range for cognitive ability. Patients with Mild Cognitive Impairment (MCI) have reported subjective memory worry independently or in consultation with their clinician. They have been placed into either the early or late phases of MCI. In the final stages of AD, dementia symptoms gradually deteriorate over many years. Therefore, early identification (Chen *et al*., 2018; Lu *et al*., 2018) is essential to prevent worsening health conditions. A probable diagnosis is based on illness and cognitive testing history with medical imaging and blood test to rule out other possible causes. Despite being effective, Neuroimaging methods are extensively suggested

diagnosing methods by medicos for early recognition of AD, like Positron Emission Tomography (PET) (Cheng and Liu, 2017) and MRIs (Lian *et al*., 2018). The Brain 3D MRI technology can provide a clear image of various brain parts than other imaging techniques. Generally, an image is gathered from the 3 Tesla T1 weighted imaged MRI scanners. This study uses 3D MRIs (Wee *et al*., 2019) baseline imageries from the AD Neuroimaging Initiative (ADNI, 2007) (http://adni.loni.usc.edu/data-samples/access-data) dataset acquired from 3 Tesla T1 weighted pictures. The T1 structural weighted MRI scans are acquired using a 1.5 T or 3T scanner. The characteristic 1.5 T gaining parameters Repetition Times (RT) = 2400 ms, Inversion Times (IT) = 1000 ms, least full Echo Time (ET), flip angle = 8°, acquisition matrix = 256×256×170 in x, y and z dimension, the Field Of View (FOV) =240×240 mm^2. Capturing voxel sizes of 1.25×1.25×1.2 mm^3. The variable acquisition value of the 3T scan is repetition time = 2300 mm, minimum full of echo time, inversion time = 900 ms, flip angles = 8°, FOV = 260×260 mm^2, acquisition matrix = 256×256×170, Capturing voxel sizes of 1.0×1.0×1.2 mm^3. The parameters are commonly utilized to capture brain MRI scans in many scan centers. For processing and produce the highest throughput from the 3D MRI brain images (Feng *et al*., 2018). There are numerous machine learning models that already exist for early AD phase identification using MRI (Vu *et al*., 2018; Beheshti *et al*., 2017; Ortiz *et al*., 2017; Shi *et al*., 2017b; Jha and Kwon, 2017) imaging. However, most existing approaches failed to forecast the early phases of Alzheimer's with minimum prediction error or loss. This research's main objectives are precise pathological biomarkers' AD identification region, reducing the overfitting issues, and optimizing the classifier's performance to reduce error/loss rate. The research contributes to filling the gaps and improving the WODSNN model's performance in AD stage identification.

Literature Review

This section deliberates the studies on MRI imaging methods and different studies on deep learning-based AD detection approaches. Table 1 describes recent studies on AD disease, which contain information about the type of data used, the name of the dataset and the number of samples and classes used, deep classifier name, contribution and limitations of the research work, and accuracy rate.

Note: Ref- Reference, Acc*-Accuracy, ROC*-Receiver operating characteristic, OASIS*-Open Access Serious of Imaging Studies, ADNI*-Alzheimer's disease neuroimaging initiative, LSTM*-Long short-term memory, DCNN*-deep convolution network, PSA*-Principal component analysis.

It is essential to avoid the limitations of the above discussed recent studies in Table 1 and to enhance the performance of the deep models to achieve AD stages detection with less loss rate. A new dermoscopic image segmentation (Ashour *et al*., 2019) approach has been introduced in this research, which uses a Neutrosophic set for segmentation. Unlike other logics, Neutrosophic uses an indeterminacy subset. The Neutrosophic images have been defined as three subsets, true, false, and indeterminacy subset. This research's comparative evaluation results analysis shows that the Neutrosophic logic-based segmentation approach has attained the highest accuracy than comparison segmentation approaches. The goal of this study (Gupta and Verma, 2020) is to transform 1-D adaptive filters into innovative 2D adaptive filters. The results of the performance evaluation show that the unique adaptive filters outperform other comparison filtering techniques, which is advantageous for reassembling the biological image. This study (Singh *et al*., 2020) proposes a new model for multiplicative noise suppressions and strong contrast improvement and demonstrates its effectiveness by utilizing a wide variety of clinical ultrasound images. The feature enlargement step of this framework improves the texture and contrast of ultrasound videos using a developed CLAHE method. The study by Damodaran *et al*. (2017) created a novel feature assortment method for classifying hyperspectral images. Aligning the empirical kernel map in the RKHS according to Surrogate Kernal and HSIC yields the 'new class separability extent. The study included feature extraction and decreased content-based picture retrieval methods (Garg and Dhiman, 2021). The method combines the Gray Level Co-occurrence Matrices (GLCM) descriptor and comprehensive structural feature extraction to extract statistical characteristics of an image's texture. Improved accuracy in the classification of the CORAL dataset is made possible using GLCM based feature extraction methods. A wavelet, transform-based feature extraction method and an evolving neural network, as described in the paper above, may now be used to discover and localize high-impendence faults in a time fluctuating distributed generation model (Lucas *et al*., 2020). In terms of dependability and accuracy, the findings of this procedure are positive. The output of the Gabor filter was used in this study (Al-Kadi, 2017) with 4 different fixed-resolution texture signatures with and without segmenting the cell nuclei to examine the magnitude responses. The best accuracy rate was obtained during testing when the energy of the Gabor filter was combined with the fractal signatures of the meningiomas in the sub-image. In this study (Fan *et al*., 2021), an improved WO has been introduced with a join search mechanism for solving low convergence rates, easy fall into local optimum, and handling high dimensional data problems in other optimizers (Darwish, 2018). Initially, it uses a chaotic tent map to maintain the initial population's diversity for global search.

Table 1: Recent research on deep learning-based ad detection

Ref.	Data	Dataset and class	Deep model	Contribution	Limitations	Acc %
Jain *et al*. (2019)	T1- MRI	ADNI and 50 AD, 50 CN, 50 MCI	VGG16	Introduced transfer learning for a feature learning using VGG16 and image	Fewer samples used for training	95.73
Liu *et al*. (2020)	T1 MRI	ADNI and 97 AD, 233 MCI, 119 NC	Multi-tasks deep CNNs +3D DenseNets	Multi-model DL for hippocampal classification-cation and segmentation	Fewer samples used for training	92.5 (ROC)
Basaia *et al*. (2019)	3D T1-MRI	ADNI 416 AD, 280 cMCI, 533 sMCI	CNN	Introduced a computer -aided system for individual diagnosis of AD and MCI	Skipped pre pro cessing, model trained with less	99
Wang *et al*. (2019)	3D MRI	ADNI and 221 AD, 297 MCI, 351 NC	Dense Net	Developed an ensemble of 3D Dense connections and probability-based fusion methods	Pathological bio markers of AD not identified before training	97.52
Wang *et al*. (2018)	3.0T MRI	The local hospital, OASIS and 98 AD, 98 HC	8 layered CNNs	CNNs with leaky ReLU, and max pooling	Overfitting issues	97.65
Ebrahimi-Ghahnavieh *et al*. (2019)	3D MRI	ADNI and 132 AD subjects	GoogleNet/ AlexNet/ VGGNet16 and19/ ResNet 18 and 15 and 101/ SqueezeNet/Inceptive3 + LSTM	Utilized different combined CNN models with LSTM to train single and multi-view mode images of AD	Complex to train obtained high prediction error	90.62
Allioui *et al*. (2020)	MRI	OASIS and 609 NC, 489 AD	PSO + CNNs	Usage of PSO in CNNs to reduce training losses	Pathological biomarkers of AD not identified before training	94.73
Li *et al*. (2020)	4D fMRI	ADNI and 116 AD, 99 MCI, 174 NC	C3D + LSTM	Established a 4D learning model for utilizing spatial and time-varying data for AD discrimination	Fewer samples used for training	92.11
Niu and Tan (2020)	MRI	ADNI and	3DCNN	Introduced residual densely connected CNN	Pathological biomarkers of AD not identified before training	94.4
Liu *et al*. (2020)	1.5 T T1 MRI	ADNI-3566 BIO CARD-744	Deep siamese neural networks	New non-linear kernel tricks are utilized to normalize the extracted feature	Skipped Preprocessing Uncertainty issues	99.86

Next, an adaptive inertia weight enhances the convergence precision speed and jumps from the local optimum. In conclusion, an opposition-based learning process updates the whale population's individuals in each iteration. The results prove that the JSWO outperforms with twenty-three benchmark functions. In this study (Saxena and Cao, 2019), researchers implicitly learned the characteristics necessary for accurate Spatiotemporal (ST) prediction using a unique deep generative adversarial network model. Autoencoders and decoders are built into this model's DGAN architecture. One of its main features is a fusion model that considers external influences and another is a deep ST feature learning model that can deal with ST correlation and stochastic aspects. The results demonstrate that the DGAN technique outperformed 14 commonly used baseline approaches in handling the ST data in terms of accuracy.

The above studies discuss the recent image processing-related methodologies and their special features, all incorporated in WODGAN to improve performance. Most existing approaches failed to forecast the early phases of AD with minimum prediction error or loss.

Therefore, these studies face certain limitations, such as improper pathological biomarker region identification and overfitting issues, reducing the classifier's performance to reduce the error/loss rate. The research contributed to fulfilling the above-discussed existing AD detection system's limitations and introduced a new AD detection approach named WODGAN. The AD detection system consists of two distinct models to train networks: A discriminator and a generator. The generator makes a fake image (by randomly choosing image samples and adding noise to them) while the discriminator uses real images as input to train the model. The AF approach is applied to eliminate noise in a real image and adaptive histogram-based image enchantment methods were employed to enhance the image's quality. Instead of whole direct MRI image-based training, the region grows. The significant biomarker features are a selection from the extracted features to reduce overfitting issues. The deep and fully

connected layer of the deep generative adversarial networks receives the combined features and uses them to train models. If the MRI image contains real AD stages, the discriminator obtains prediction loss to determine validity. Each time the discriminator meets fake images of the generator (high losses), the discriminator and the generator's network nodes are back-propagated to retrain the model. The optimizer in DGAN helps reduce the prediction error and improves network performance. The methods of WODGAN and their functionalities are discussed in the subsequent section.

Methods of Wodgan-Based Ad Stages Recognition

Figure 1 demonstrates the AD recognition procedure of the WODAN model; in line with the AD recognition system, 3D MRI brain images had initially been gathered from several dataset sources.

Functionalities are discussed in the subsequent section. But, first, the approach is utilized to segment exact biomarker regions, and various texture feature extraction approaches are applied to extract feature information.

The discriminator uses actual pictures as training data, while the generator produces test data by randomly selecting image samples and adding noise. The preprocessing stage consists of image filtering, enchantment, region growing based biomarker regions segmentation, biomarker feature extraction techniques, and significant biomarker feature selection. Next, when features are consolidated, they train a deep generative adversarial network consisting of several layers. The discriminator then uses the likelihood to determine the prediction loss, which it uses to determine whether or not the phases shown on the MRI are associated with AD. Finally, the DGAN nodes are back propagated using a whale optimizer when the discriminator identifies a false generator image (based on losses), retraining the generator model and a generator until the model learns real AD stages. This section explores the WODGAN methods and their features.

In contrast to existing deep learning models, the proposed WODAN model includes a distinct step for segmenting biomarker regions where densenet with ensemble technique, 3DCNN, PSO + CNNs fails to handle this biomarker regions identification before training. Skipped preprocessing steps in deep Siamese neural networks and CNN leads to drawbacks. It enables the model to concentrate on pertinent brain areas linked to Alzheimer's disease. The model may increase its recognition and discriminating abilities by utilizing texture features. The WODAN model updates and retrains the generator using backpropagation and a whale optimizer. Existing approaches like CNN ReLU couldn't handle uncertainty issues, thus leading to overfitting issues. Here we are solving uncertainties with the help of fuzzy neutrosophic logic.

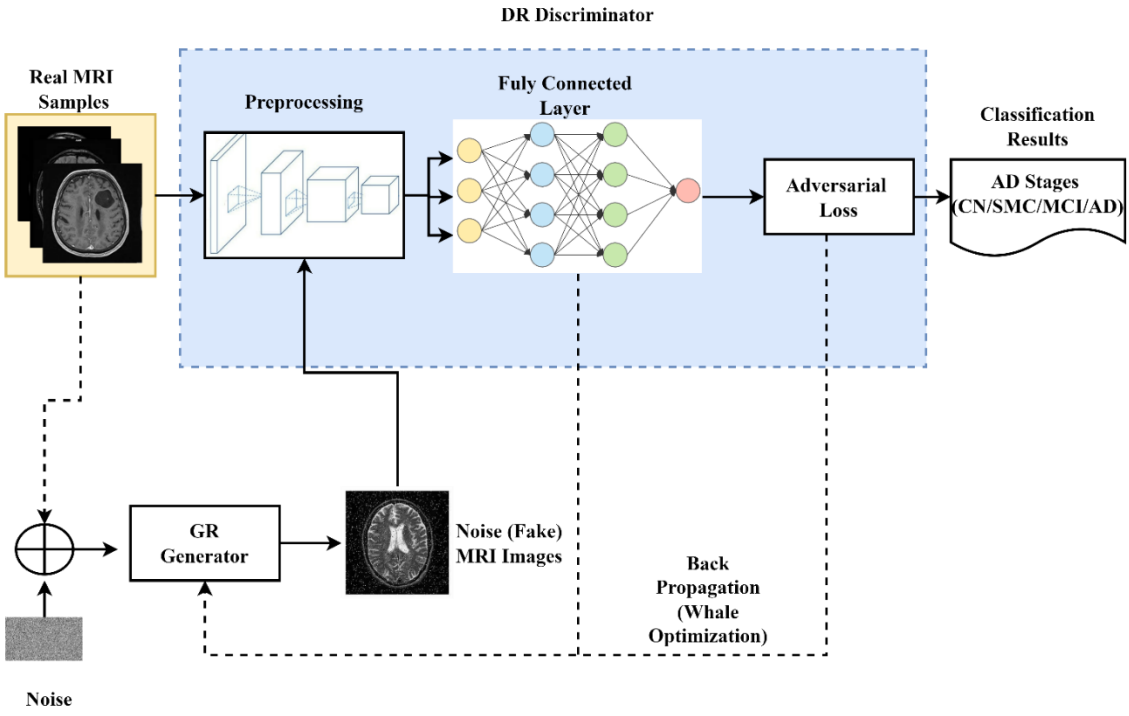

Fig. 1: The architecture of WODGAN-based AD stages detection

Table 2: Overall class-wise Alzheimer's images

	Stages/classes of AD			
Samples (MRI Imageries)	CN	SMC	MCI	AD
Total samples	1067	550	1191	968
Training	801	413	894	727
Testing	266	137	297	241

3D MRI Data Acquisition

In this research, the following benchmark, Alzheimer's datasets, are utilized for training the AD detection models. The overall AD dataset images contain 4 classes: CN, SMC, MCI, and AD. The MRI imageries are gathered from different datasets, which are discussed here. The imbalanced value in Table 2 is chosen since we are employing various datasets from which the MRI images were obtained to analyze different stages of AD.

Alzheimer's Disease Neuroimaging Initiative (ADNI) database (ADNI, 2007) is classified into 4 categories of database ADNI-GO (Grand Opportunity), ADNI-1, ADNI-3, and ADNI-2. When combined, ADNI-1 and ADNI-GO have 400 SMC, 400 MCI, and 200 AD. 150 MCI, 150 ND, 150 AD, and 150 SMC comprise ADNI-2. 133 ND, 151 MCI, and 87 AD are in the ADNI-3. More than a thousand people's information is stored in the database for the Australian Imaging Biomarker and Lifestyle flagship study of aging (AIBL) (AIBL Study ADNI Data, n.d.) (https://aibl.csiro.au/adni/index.html). Images of AD, MCI, and CN are included in the collection. Almost a thousand people contributed to the Open Access Serious of Imaging Studies (OASIS) dataset (Marcus *et al*., 2007). The database includes MRI images from 609 individuals with CN and 489 with MCI. MIRIAD (NITRC: MIRIAD) Minimal Interval Resonance Imaging in Alzheimer's disease: Tool/Resource Info, n.d.) (https://www.nitrc.org/projects/miriad) is a dataset of volumetric MRI brain scans of 46 AD and 23 healthy persons. The dataset contains 708 brain scan images.

Table 2 contains overall images used for the analysis and prediction of phases of AD. This study uses 3775 MRI brain scan images to evaluate the AD detection model. The model training and testing processes have been utilized in 75 and 25% of images.

Adaptive Filtering

Noise elimination is an important phase in preprocessing to reserve MRI pictures' biomarkers (brain neurons); it aids in improving prediction performance. The white Gaussian noises in MRI images decrease forecasting accuracy. Hence, this Classification model also incorporates an AF method to reduce the noise. The AF method creates better filtering outcomes than linear filtering. It conserves edges and other high-frequency portions of MRI pictures. The statistical derivation of the AF is expressed by:

$$\hat{f}(a,b,c)=g(x,y,z)-\left(\frac{\sigma_{\eta}^{2}}{\sigma_{L}^{2}}\right)[g(a,b,c)-m_{L} \quad (1)$$

where, in (Eq. 1) the σ_{η}^{2} indicates the total noise, σ_{L}^{2} signifies the local variance of local regions, m_L represents local means, and $g(x, y, z)$ symbolizes the noisy picture's voxel value at the location (a, b, c). The notations S_{η}^{2}, S_{L}^{2} indicate local variance and noise variance of the particular area s_{xy} correspondingly.

The generator may explore a wider variety of image variations and create diverse and excellent synthetic images by constantly modifying the filtering algorithms with different input patterns that can be used to adjust the weights of adaptive filters. The filter parameters can be changed to produce more realistic and aesthetically pleasing images by considering the individual features and structures found in the data. Deep networks can perform numerous filtering activities, like edge detection, texture extraction, and feature development, without drastically distorting the images since they use convolutional layers. Convolutional filters are local, which enables the network to concentrate on capturing tiny details while preserving the general shape and layout of the input image. However, the deformation is limited in early layers where local filtering processes occur, allowing the networks to perform filtering tasks while maintaining picture integrity efficiently.

The subsequent three conditions enable filtering noise and preserving the biomarkers' edge:

Condition i : *if* $(s_{\eta}^{2}=0)$, return values of $g(x, y, z)$

Condition ii : $(s_{L}^{2}>s_{\eta}^{2})$, return values close to $g(x, y, z)$ (high local variance associated with the edge is conserved)

Condition iii : *if* $(s_{L}^{2}=s_{\eta}^{2})$ return arithmetic mean m_L

Filtering the noises in MRI images using (Eq. 1) based on the three requirements above has been shown to reliably maintain the edges of biomarkers, even though MRI imaging noise is a widespread problem. Image enhancement follows the convolution layer as a crucial intermediate step.

Adaptive Histogram Equalization

The sliding window AHE methods were used in the framework for image improvement. Contrasting other equalization methods, it makes a lot of histograms. Every one resembles a different part of the MRI imageries and these are used to reallocate the lightness values of MRIs. Consequently, it enhances local contrast and brings out the boundaries in MRI brain pictures. When tiling an image, it just adjusts the histogram for each voxel by adding up the new row of voxels and deducting the row

that was left behind. The rectangle voxel is moved at a time. This lowers the computational histogram complexity from O (N_2) to O (N). indicates the next rectangle's width. Every voxel is altered to boost AHE using transformation functions that take into account its surroundings. Because every voxel is altered according to the histogram of the square around it, this can simplify things. The better MRI image that resulted was then used as the input for noise filtering. The left side sample MRI brain images and the right-side standardized histogram curve of an image are shown in (Fig. 2). Improving the image quality is made easier by the AHE peak points.

Region Growing-Based Segmentation Using Fuzzy Neutrosophic Logic (Rgsfnl)

The enhanced MRI image has been taken to identify the AD stages related to pathological region-based biomarkers regions using the Fuzzy neutrosophic logic region growing approach. In logic, each proposition is estimated to have the Degree of Truth (DT), Degree of Indeterminacy (DI) (neither true nor false), and the Degree of False (DF), which are all called neutrosophic logic, where DT, DI, and DF are a neutrosophic Component. The main advantage of this logic over fuzzy logic is that it brings indeterminacy DI to estimate DT and DF's value. In this research, the region-growing approach defines the degree of false DF = 1-DT. Therefore, every pixel must calculate the DT and DI, respectively, and decide whether the pixel belongs to the biomarker region based on DT and DI values. The mathematical derivation for the degree of DT and DI is derived as follows:

$$\begin{cases} DT(m,n,o)=1-\dfrac{\left|f(m,n,o)-\overline{f_R}\right|}{f_R} \\ DT'(m,n,o)=1-\dfrac{\left|\overline{f_{mno}}-\overline{f_R}\right|}{f_R} \\ DI(m,n,o)=1-e\dfrac{var(f_{mno})}{100} \end{cases} \quad (2)$$

where, (Eq. 2) $f(m,n,o)$ denotes the intensity value of pixel (m,n,o), $\overline{f_R}$ denotes the intensity mean of all pixels in the current biomarker region. The $\overline{f_{mno}}$ $var(f_{mno})$ and are intensity mean and variance of small circles region (each pathological biomarker region of the brain) centered at pixel (m,n,o), respectively. $DT(m,n,o)$ and $DT'(m,n,o)$ can be used to examine the variations between the current pixel and pathological biomarker region's mean. (Eq. 2) is used as a region-growing criterion to decide whether the current pixel should be added to the pathological biomarker region. In a homogeneous region, the criterion $DT(m,n,o)$ confidence is used to justify whether a pixel belongs to the pathological biomarker region or not. In a noisy region, the criterion $DT(m,n,o)$ is not confident because the current pixel intensity range becomes high due to noise effects. In such a case, it requires another criterion $DT'(m,n,o)$ to decide whether or not the current pixel belongs to the pathological biomarker region. According to the analysis, a low DI denotes that a pixel belongs to a homogeneous region and a high DI denotes that the pixel belongs to a noisy region. When a DI becomes high and low the $DT'(m,n,o)$ and $DT(m,n,o)$ the region has been used, respectively.

Figure 3 shows segmented MRI brain imageries of phases of AD that are based on fuzzy neutrosophic logic. The blue color denotes the segmented various biomarkers regions of AD.

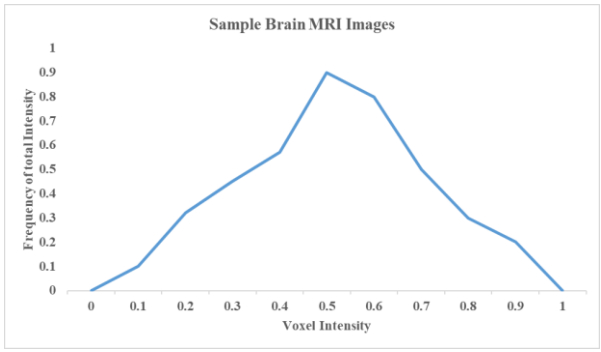

Fig. 2: Sample AHE outcomes

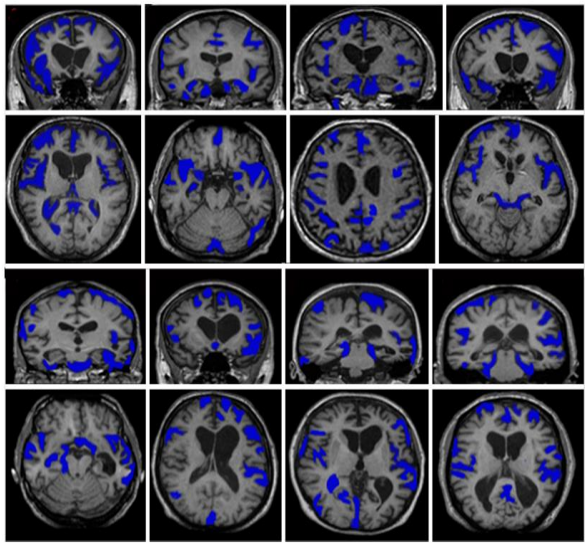

Fig. 3: Segmented biomarkers regions of AD stages

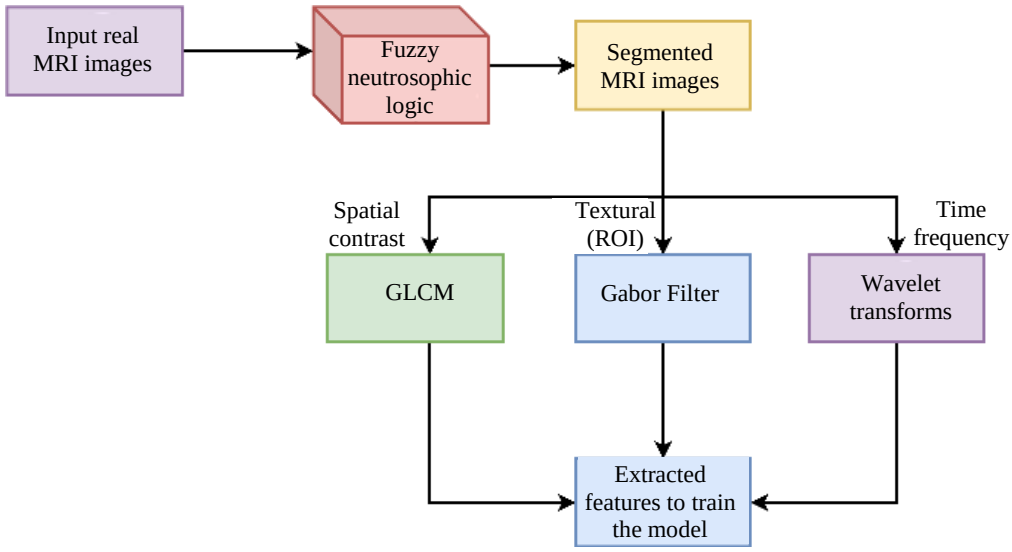

Fig. 4: Block diagram of feature integration

Algorithm: Fuzzy neutrosophic logic-based segmentation

Input: Quality Enhanced real MRI brain image
A= imread (data source)
[m,n,o] = Size(A)
For each i=1 to m
For every j=1 to n
For every k=1 to o
Seed= pick_from_region() // *selecting seed point*
IF ((DI(m,n,o) < threshold_1 && DT(m,n,o) >= threshold_2) || (DI(m,n,o) < threshold_1 && DT'(m,n,o) >= threshold_3))
Region[m,n,o]=f(m,n,o) // *add current pixel in current region*
Update $\overline{f_R}$ // *update region mean*

End IF
End For
End For
End For
Output: Segmented MRI grayscale image

The algorithm explained how the Fuzzy neutrosophic logic DI, DT, and DT's confidence rules help the region's growing segmentation of homogeneous biomarker regions. Finally, the segmented biomarker areas are extracted for biomarker features to train the model.

Feature Extraction

The segmented biomarker areas of the brain are used to extract the MRI biomarker features using a variety of feature extraction approaches. The biomarker data from the MRI images used in this investigation were extracted using the GLCM, wavelet, and Gabor features, as shown in Fig. 4. GLCM feature is used to extract the numerical features of a texture utilizing spatial associations of comparable grey tones:

$$Contr=\sum_{r=1}^{N\,gl}\sum_{c=1}^{N\,gl}|r-c|^2\,GM\,(r,c) \tag{3}$$

where, in (Eq. 3), the symbol *Ngl* indicates the discrete grey levels, *r* denotes the row, *c* symbolizes the columns, and *GM*(*r*, *c*)-GLCM. The contrast feature values of *M* images are extracted using it:

$$Corrm=\frac{\sum_{r=1}^{Ngl}\sum_{c=1}^{Ngl}(rc)GM\,(r,c)-\mu_x\,(r)\,\mu_y\,(c)}{\sigma_x\,(r)\,\sigma_y(c)} \tag{4}$$

where, in (Eq. 4) symbol $\mu_x(r)$ and $\mu_v(c)$ denotes the mean of rows and columns, $\sigma_x(r)$ and $\sigma_v(c)$ denotes the standard deviation of the rows and columns utilized to extract the relationship feature values of MRI images:

$$Entr=-\sum_r\sum_c GM\left[r,c\right]ln(GM\left[r,c\right]) \tag{5}$$

where, (Eq. 5) is utilized to calculate the entropy values of MRI images. The $GM\left[r,c\right]$ denotes the grey tone spatial dependence matrices, the r,c indicates the row and column value and *Ngl* is the number of distinct grey levels in quantized images:

$$Clust\,Pro=\sum_{r=1}^{Ngl}\sum_{c=1}^{Ngl}\left[r+c-\mu_x\,(r)-\mu_y\,(c)\right]^4\,GM\,(r,c) \tag{6}$$

$$ClustShade=\sum_{r=1}^{Ngl}\sum_{c=1}^{Ngl}\left[r+c-\mu_x\,(r)-\mu_y\,(c)\right]^3\,GM\,(r,c) \tag{7}$$

$$ClustTen=\sum_{r=1}^{Ngl}\sum_{c=1}^{Ngl}\left[r+c-\mu_x(r)-\mu_y(c)\right]^2 GM(r,c) \quad (8)$$

where, (Eqs. 6-8) are utilized to compute the cluster shade, cluster prominence, and cluster tendency value of the segmented biomarkers areas. The variable μ_x indicates the mean of rows and μ_y Signifies the mean of columns. The GLCM-based mathematical relationships of different texture feature data of the biomarker texture are extracted to train models:

$$AC=\sum_{r=1}^{Ngl}\sum_{c=1}^{Ngl} rcGM(r,c) \quad (9)$$

Equation 9, the notation *'r'* denotes the row, *'c'* denotes the column and the *Ngl* represents the number of discrete grey levels. (Eq. 9) calculates the autocorrelation of texture features:

$$DS=\sum_{r=1}^{Ngl}\sum_{c=1}^{Ngl}|r-c|GM(r,c) \quad (10)$$

Equation 10 calculates the dissimilarity ratio of a homogeneous or heterogeneous segmented region's texture information:

$$DE=\sum_{a=0}^{Ngl-1} GM_{r-c}(a)log_2\left[GM_{r-c}(a)\right] \quad (11)$$

Equation 11 calculates the difference entropy value segmented region's texture information.

Input is taken from Quality Enhanced real MRI brain image. The improved MRI picture has been acquired to identify the AD phases associated with diseased area-based biomarkers regions with the Segmented MRI grayscale image as output using the fuzzy neutrosophic logic region growth approach. The output images need to be enhanced by extracting features GLCM, wavelet, and Gabor filtering features. GLCM is first applied to extract numerical features from the texture with the spatial combination of grayscale images. Then Gabor filter captures the textural qualities and energy distribution found in the image. These texture features based on Gabor energy can be derived from certain image regions of interest or biomarker textures. Then, for various tasks, including segmentation and classification, these features are utilized to train machine learning models. Computational models for classifying and analyzing medical disorders can be taught by extracting Gabor filter characteristics from medical images. A wavelet filter for performing various scale analyses on signals and images. It breaks down a signal or image into various frequency bands, enabling the simultaneous analysis of both high- and low-frequency components. The wavelet provides a multi-resolution image of the data transformation, incorporating local and global information. Finally, extracted details are used to train the model.

Incorporating these techniques within the suggested strategy intends to take advantage of each technique's advantages to improve segmentation performance. The fuzzy technique addresses the uncertainty and imprecision for superior segmentation results, while the wavelet transform and Gabor filtering extract pertinent features and texture information.

Gabor Filter Feature

The mathematical proof of feature extraction using a Gabor filter is shown below:

$$Enr_k=\frac{1}{rc}\sum_{x=0}^{r-1}\sum_{y=0}^{c-1}\left|I_f(x,y)\right|^k \quad (12)$$

where, (Eq. 12) represents the traditional technique for extraction of Gabor filter-based texture features, the energy Enr_k, k = 1, 2, 3 in the form of l_1 and l_2 norms. The Gabor energy-based texture feature data on the biomarker texture extracted to train models. The notation r and c are the sizes of the sub-band intensities $I_f(x, y)$.

Wavelet

The basic notion of discrete wavelet transform is to bring the time-frequency representation. The two-dimensional discrete wavelet transform indicates images regarding a set of dilated and shifted wavelet functions ω^{LH}, ω^{HL}, ω^{HH}, and scaling function ϕ that form orthonormal basics for L^2 R^2. Provided J-scale discrete wavelet transform, images $x(r,c)$ of M × M is decomposed by:

$$x(r,c)=\sum_{p,o=0}^{N,q^{-1}}\mu_{p,q,o}\phi^{\vec{s}}\,p,q,o(r,c)+\sum_{B\in B}\sum_{j=1}\sum_{q,o=0}^{M-1} w^B\,p,q,o\omega^B\,p,q,o(r,c) \quad (13)$$

with:

$$\phi^{\vec{s}}\,p,q,o(r,c)=2^{\frac{-p}{2}}\phi(2^{-2p}s-q,\,2^{-p}t-o),\quad \omega^B\,p,q,o(r,c),\omega^B\,p,q,o(r,c) \quad (14)$$

$$2\frac{-p}{2}\omega^B(2^{-p}s-q,2^{-p}t-o),B\in B,B$$

where, values of M are signified as $M_p = M / 2^p$, and (Eq. 13) is utilized for the decomposition of the image $x(r,c)$ and (Eq. 14) is utilized to represent the derivative of the scaling functions. The HL, LH, and HH are entitled wavelet or DWT sub-bands in this research. $u_{p,q,o}=\int\int x(r,c)\phi p,q,odsdt$ is a scaling coefficient and $w^B_{p,q,o}=\int\int x(r,c)\omega^B p,q,odsdt$ denotes the $(q,o)^{th}$ wavelet coefficient in scales p and sub-bands B. The derivation of wavelets in (Eqs. 13-14) enables wavelet feature data extraction to train the model.

HSICL-Based Feature Selection

The *HSIC*L method works effectively with both high and low dimensional data sets. As a result, the framework employs the *HSICL* technique to reduce less-important or more-important features from the set of retrieved MRI biomarker features. The optimal *HSICL* expression is as follows:

$$HSICL: min \frac{1}{2} \sum_{NN,m=1}^{o} a_{NN} a_m HSIC(f_{NN}, f_m) - \sum_{NN}^{O} =_1 a_{NN} HSIC(f_{NN}, c) + \lambda \|a\|_{1,} a_1, ..., a_n > 0, \quad (15)$$

The (Eq. 15) is also written as follows:

$$HSICL: min \frac{1}{2} \left\| L' - \sum_{NN}^{O} =_1 a_{NN} K'^{(NN)} \right\|_F^2 + \lambda \|a\|_{1,} a_1, ..., a_o > 0 \quad (16)$$

Equation 16 is utilized to decrease important features from the different extracted MRI biomarker features. Where $HSIC(f_{NN}, c) = tr(K'^{(NN)} L')$ denotes kernel-based independence measures termed the observed *HSIC*, *tr*(.) indicates the trace, λ denotes the regularization variable, $K'^{(NN)} = \Gamma K^{(NN)} \Gamma$ and $L' = \Gamma L \Gamma$ are inputs and outputs centered Gram matrix of MRI biomarker feature. $K_{i,j}^{(NN)} = K(u_{NN,i}, u_{NN,j})$ and $L_{i,j} = L(c_i, c_j)$ are Gram matrix, $k(u, u')$ and $L(c, c')$ are the two kernel functions. $\Gamma = I_O - \frac{1}{0} 1_O 1_O^T$ denotes the centering matrices, and I_o indicates the *o*-dimensional identity matrices (number of biomarker features). I_o denotes *m* dimensional vectors every once and $\|.\|_1$ is l_1-norms. The over-fitting problem in the original recognition model is mitigated by the *HSIC* method used in the AD recognition system, which determines the bare minimum of biomarker features to train models.

Deep Generative Adversarial Network

In this study, a DGAN has been utilized to predict the AD stages. For better prediction accuracy, a Generative Adversarial Network (GAN) competes with two neural networks against one another in a competitive ML model. To learn, most GANs operate unsupervised and use a cooperative zero-sum game structure. A Generative Adversarial Network (GAN) is a form of generative modeling that uses an original dataset as input to produce new, believable results via machine learning and pattern discovery. To train generative models, GANs imitate a supervised learning process. Generator *GR* aims to generate MRI images resembling true data distribution samples. Discriminator *DR* aims to distinguish between MRI image samples created from *GR* (fakes) and those produced from the actual data distribution (original).
The *DR* assigns a higher likelihood to actual MRI imageries and a lower likelihood to the MRI photo samples produced by the generator *GR*. Generative adversarial network training continues to try to remove the produced MRI samples from the original data by utilizing the gradient data that the *DRs* provide. The MRI image s is created using the genuine picture distributions, *q* data, noise vectors, q_z, and q_g, which stands for the *GR's* distributions over the picture s. In order to get hidden vectors *z* as close to *GR*(*s*) as possible, GR uses them as inputs and outputs for samples *GR*(*z*). Because *DR*(*s*) = 0 *ifs* q_g and *DR*(*s*) = 1*ifs* q_{data}, *DR* is a classifier. Both *DR* and *GR* models are trained with a min-max purpose to address the following problems:

$$DR(s) = log + E_{zq_z} \left[log(1 - DR(GR(z))) \right] \quad (17a)$$

$$V(GR, DR) = \max(\theta_{DR}) \min(\theta_{GR}) \quad (17b)$$

V(GR, DR) represents the maximum and minimum binary cross-entropy functions generally exploited in binary classification issues. The *GR* and *DR* are trained by backpropagating losses in expression (17) via their corresponding model update variables. Owing to the two various purposes in (Eq. 17a-b), the update rules are described by:

$$\left\{ \theta_{DR}^{t+1,}, \theta_{GR}^{t+1,} \right\} \leftarrow \begin{cases} update if DR(x) predicts wrong \\ update if DR(GR(z)) predicts wrong \\ update if DR(GR(z)) predicts correct \end{cases} \quad (18)$$

where, (Eq. 18) $\theta_{DR}^{t+1,} \wedge \theta_{GR}^{t+1,}$ indicates the corresponding variables for *DR* and *GR* as well as t, the number of iterations. *DGAN* has recently gained recognition as an avant-garde technique for learning generative models of complex problems, similar to an adversarial loss.

Adversarial Losses

In D-GAN, the adversarial loss LDR_{GAN}^{DR} is derived as follows:

$$L_{GAN}^{DR} = \left\| DR(y_{real}) - 1 \right\|_2^2 + \left\| DR(y_{fake}) - 0 \right\|_2^2 \quad (19)$$

In expression (19), the adversarial losses are utilized to discover *DR* and *GRs* and stability during adversarial training. *GR* tries to reduce the *DR*(y_{fake}) with true labels to reduce the GR loss L_{GAN}^{GR}. *GR's* aim is to make real duplicate sample images for *DR*, thus, reducing the *GR* loss LDR_{GAN}^{DR}, *GR* attempts to decrease the variance between *DR*(y_{Fake}) and true labels:

$$L_{GAN}^{DR} = \left\| DR(y_{fake}) - 1 \right\|_2^2 \tag{20}$$

The total aim of the deep generative adversarial network is articulated as follows:

$$L_{DGAN} = L_{GAN}^{GR} + L_{GAN}^{DR} \tag{21}$$

where, (Eq. 20) is used to reduce the loss variance between the real labels and the *DR's* false label, and (Eq. 21) is used to calculate the total loss for the deep generative adversarial network, which is used to replace the traditional binary classification loss value of the *DR* and *GR* in expression (17). Then, *DR* and *GR* are trained by backpropagating the loss with optimizers' help via their corresponding model update variables. Training a *GAN* is difficult for several reasons, even though it has shown great effectiveness in creating realistic images. They include difficulties in model collapse, convergence, and the vanishing gradient. In this study, a whale optimizer is utilized in *DGAN* to reduce the convergence difficulties and as well as to avoid vanishing gradients problems.

Optimizer

DR and GR are trained by backpropagating the loss value with the optimizer's help through their corresponding model update variables. In this research, the DGAN loss has been backpropagated with the help of a whale optimizer. The exceptional hunting way of the humpback whale is measured as the major interesting point of these whales, stated as bubble net feeding methods. The statistical formation of WOA is as follows.

Searching for Prey/Searching for Optimal Loss

They are $\vec{A}$ denoted as random values between the interval [-1, 1] if $\left|\vec{A}\right| > 1$ then it performs a global search mechanism:

$$\begin{cases} \vec{D} = \left| \vec{C}.\vec{S}_{rand} - \vec{S} \right| \\ \vec{S}(t+1) = \vec{S}_{rand}(t) - \vec{A} * \vec{D} \end{cases} \tag{22}$$

where, (Eq. 22) $\vec{S}_{rand}$ denotes the random position vector. $\vec{A}$ and $\vec{C}$ is considered the coefficient vector, $\vec{D}$ denotes the distance vector, and the symbol $\vec{S}$ denotes absolute value. The search agent updates their positions randomly in each iteration by selecting search agents that are yet determined. The variable range of the $\vec{A}$ search agent is from 2-0. The agent has been chosen when $|A| > 1$. The searching for prey model uses the DGAN approach to search for optimal network loss.

The humpback whales' complex patterns of sound and movement, which they use to coordinate and communicate while hunting, served as the model for the WO algorithm. To enhance the effectiveness of the GAN model, the algorithm replicates this behavior and iteratively adjusts its settings. It fine-tunes the network parameters, enabling the GAN to recognize and learn the biomarker regions and patterns corresponding to various stages of AD. As a result, the model can more accurately identify and categorize AD-related photos. The WO algorithm can be incorporated into the GAN model to boost its ability to produce realistic visuals that closely mimic real AD-related patterns. The GAN model may be able to converge to better solutions by adding the WO algorithm during the training process, resulting in increased picture production and discrimination capabilities. The proposed model may increase the precision of AD stage recognition by optimizing the GAN using the WO algorithm. The improved network can learn and distinguish the biomarker regions that correspond to the various phases of AD better, enabling more accurate and reliable disease diagnosis. The WO method adjusts the model's parameters depending on the discriminator's assessment of produced and real images to optimize the network.

Bubble Net Attacking / Select Optimum Loss

Surround the Prey

The main objective of this encircles the prey is obtaining the optimal candidate solution. The statistical derivation of the optimal candidate solution is represented by:

$$\vec{S}(t+1) = \vec{S}(t) - \vec{A} * \vec{D} \tag{23}$$

$$\begin{cases} D = \left| \vec{C}.\vec{S}(t) - \vec{S}(t) \right| \\ \vec{A} = 2\vec{a} * \overrightarrow{rand} - \vec{a} \\ \vec{C} = 2 * \overrightarrow{rand} \end{cases} \tag{24}$$

where, in (Eq. 23), '*t*' signifies the iteration of a current position, $\vec{A}$ and $\vec{C}$ is measured as the coefficient vector. The '$\vec{S}$' ' denotes the position vector of the current optimal solutions and the symbol $\vec{S}$ denotes absolute value. The " denotes the element-wide multiplication. Equation 23 is used to find the optimal candidate solutions. In (Eq. 24), the notation $\vec{a}$ value has been chosen from 2-0 for each iteration and $\overrightarrow{rand}$ is stated as a random vector in the interval of [0, 1]. The humpback whale hunts the prey utilizing the bubble nets approach.

Spiral Updating Position

$$\vec{S}(t=1) = \vec{D'}.e^{bi}\cos \tag{25}$$

where, in (Eq. 25) the $\vec{D'} = \left| \vec{S}(t) - \vec{S}(t+1) \right|$ denotes the distance of i^{th} whale to prey, e^{bi} the *bi* denotes the

constant and *n* indicates the random numeral between the interval [-1,1]:

$$\begin{matrix}\vec{S}\\ \vec{S}(t)-\vec{A}*\vec{D}, if q<0.5\\ \vec{D}'.e^{bi}.\cos(2\pi n)+\vec{S}(t), if q<0.5\\ \vec{S}(t+1)=\vec{S}(t)-\vec{A}*\vec{D}\end{matrix} \quad (26)$$

In (Eq. 26), *'q'* is denoted as the random values between the interval [0, 1]. During the optimization, whales swim around the prey in shrinking circles order with the likelihood of 0.5% of choosing spiral model orxcc to encircle the prey approach to update whale position, derived in (Eq. 26). The Bubble net attacking approach of WOA has been utilized in the DGAN model to select optimum network nodes and back-propagate during loss values updating. In this research, prey is considered as the loss value of nodes, and the whales are considered various node features.

Pseudocode: WODGAN-Based AD Detection for Discriminator

Step 1: Gather input data source
Initialize parameters for AE, AHE, and ROI.
Step 2:
For every j=1 to TNF
gabor [*j*,*i*] = imgaborfilt(Region of Interest)
wavelet [*j*,*i*] = wav_fea(Region of Interest)
For GLCM update GLCM_feature1(ROI)
update contr, corn, autocorr, dissim for all *i*,*j*
End For
End For
Step 3:
Reduct_set = HSICL(FV)
FV = Reduct_set
Step 4:
For every t=1 to m
For each h=1 to n
Rl= φ (W. FV(t) + U. h + bi)
Step 5:
If ($Rl>-1$) & ($Rl<1$)
For every t=1 to Iterations
$L_{DGAN}=L_{GAN}^{GR}+L_{GAN}^{DR}$
If (L_{DGAN} <=Rl)
$O_t = SMC \| CN \| MCI \| AD$
Else If ($L_{GAN}^{DR}>Rl$)
$FV(t+1) = L_{DGAN}$
$FVR(t+1)=FV(t)-\vec{A}*\vec{D}\|\vec{D'}.e^{bi}.\cos$
End For
End If

Pseudocode: WODGAN-Based AD Detection for Generator

Gather data source
Assign h = 0, bi = U = 0.001;
Step 1:
For every j = 1 to TNF
gabor [j,i]= imgaborfilt(Region of Interest)
wavelet [j,i]= wav_fea(Region of Interest)
Update GLCM features
End For
Step 2:
For every t=1 to m
For every h=1 to n, do **step 3**
Step 3:
If (Rl >-1) &&(Rl <1
For every t=1 to Iterations
$L_{DGAN}=L_{GAN}^{GR}$
End If
If ($L_{GAN}^{GR}>Rl$)
$FVF(t+1) = L_{DGAN}$
$FVF(t+1)=FV(t)-\vec{A}*\vec{D}\|\vec{D'}.e^{bi}.\cos$
End If
End For

Based on the pseudocode, the AD stage is predicted. The above Pseudo code shows the step-by-step execution process of the WODGAN classifier. First, the classifier is evaluated with 3D MRI brain images, which have been gathered from many database sources. The preprocessing step consists of image filtering, image enchantment, region-growing-based biomarker regions segmentation, biomarker feature extraction techniques, and significant biomarker feature selection. Next, the consolidated feature is fed into the full and deep layer of the DGAN to train models. Finally, the discriminator determines whether the MRI images are genuine AD stages or the generator's fake images by computing the likelihood of knowing the forecasted losses. The generator model is retrained whenever the discriminator finds false images of the generator (losses), and a generator up to the model acquires real AD stages.

Classification and Segmentation Validity Metrics

Partition Entropy (PartEnt):

$$PartEnt=\frac{-1}{TPS}\sum_{r,s=1}^{k}\varphi_{rs}\log_2\varphi_{rs} \quad (27)$$

where, φ_{rs} mean the segmented region and *TPS* the total number of pixels in a specific segmented region.

Partition Coefficient (PartCo):

$$PartCo = \frac{1}{TPS}\sum_{r,s=1}^{k}\varphi_{rs}^{2} \quad (28)$$

φ_{rs}^{2} mean square of the segmented region and TPS represents the total number of pixels in a specific segmented area. *r* and *s* denote the sample position of the segment.

Dice:

The pairwise overlap of repeated segmentation is calculated using Dice:

$$Dice = \frac{2TrPo}{2TrPo + FaPo + FaNe} \quad (29)$$

where, *Trpo-Truepositive*, *FaPo-Falsepositive*, *FaNe-FalseNegative*.

Accuracy (Acc):

$$Acc = \frac{TrPo + TrNe}{TrPo + TrNe + FaPo + FaNe} \quad (30)$$

TP-True Positives, *TN-True Negatives*, *FP-False Positives*, *FN-False Negatives*.

Recall (Rec):

$$Rec = \frac{TrPo}{TrPo + FaPo} \quad (31)$$

It is otherwise called sensitivity.

Precision (Pre):

$$Pre = \frac{TrPo}{TrPo + FaNe} \quad (32)$$

It is otherwise called specificity.

Multi-Class log loss $MC_{LogLoss}$:

$$MC_{Log\,Loss} = -\sum_{L=1}^{tc} a_o, L\ log\,(p_o, L) \quad (33)$$

where,

tc' = Total number of Alzheimer's stages (class labels)
$'p_o'$ = Probability observation of the predicted Alzheimer's stage (class)
a_o = Correctly predicted Alzheimer's stage (class label) of the observation *'o'*
L = Class labels of Alzheimer's stages (AD/ CN/ SMC/ MCI)

Mean Square Error (MSE):

$$MSE = \frac{1}{TNS}\sum_{j=1}^{TNS}(AC_j - \hat{P}C_j)^2 \quad (34)$$

N = Total number of MRI image samples
AC_j = Actual Alzheimer's class
$\hat{P}C_j$ = Predicted Alzheimer's class

Mean Absolute Error (MAE):

$$MAE = \frac{1}{TNS}\sum_{j=1}^{T\,N\,S}\left|AC_j - \hat{P}C_j\right| \quad (35)$$

$\vec{S}$ denotes the absolute value.

The effectiveness of the WODGAN model is assessed, and biomarker regions are segmented in AD detection phases utilizing brain MRI images, employing the aforementioned metrics (Eqs. 27-35). The evaluation results of the WODGAN model have been explained in the succeeding section.

Results and Discussion

This section deliberates on the performance assessment of the novel AD recognition model. first, the WODGAN model's excellence is identified with different classification assessment metrics of accuracy (Haq *et al*., 2018; Liu *et al*., 2020; Niu and Tan, 2020) and the loss/error rate, like accuracy, precision, recall, mean absolute errors and mean square errors, and multi-class log loss. Second, the segmentation accuracy is estimated with various accuracy metrics such as Partition entropy (Parent), Partition Coefficient (Part Co), and Dice index. Third, the AD phases categorization model has been executed in MATLAB simulators. Finally, the system performance is compared with current deep classifiers like 8-Layered CNN (8LCNN), Deep Siamese Neural Network (DSNN), DenseNet, and VGG16.

Table 3: Segmentation accuracy

	RGSFNL			
Metrics name (%)	CN	SMC	MCI	AD
$\vec{S}$ *PartEnt*	99.4	98.2	99.6	99.7
Part Co	98.7	98.1	98.2	98.2
Dice	98.9	97.4	99.3	99.5

Table 3 contains information about AD stages-wise segmentation accuracy rate comparison for region growing segmentation fuzzy neutrosophic logic. It shows that the $DT(m,n,o)=1-\frac{\left|f(m,n,o)-\overline{f_R}\right|}{f_R}, DegreeofTrue'(m,n,o)$ and $=1-\frac{\overline{f_{mno}}-\overline{f_R}}{f_R}$ the degree of indeterminacy $DI(m,n,o)=1-e\frac{var(f_{mno})}{100}$ rules of fuzzy neutrosophic logic help to segment the various pathological biomarkers regions precisely with a maximum of 99.7, 98.7, and 99.5% accuracy rate for partition entropy, partition coefficient, and dice index, respectively.

Table 4 contains information about the consolidated performance comparisons of the WODGAN model with four recent high throughput class fiers for AD stage identifications, such as VGG16, DN, 8LCNN, DSNN, and WODGAN. According to the table values, the WODGAN has obtained a high 99.92% accuracy ratio and 0.08% lesser loss ratio in AD stages detection.

Figure 5 illustrates the multi-class log loss curve comparison for the detection of WODGAN, DSNN, 8LCNN, DN, and VGG16 models in AD stages. It attests that the adversarial loss function $\left(L_{DGAN}=L_{GAN}^{GR}+L_{GAN}^{DR}\right)$ incorporated with the deep discriminator model in WODGAN helps in obtaining less loss rate than existing classifiers.

Fig. 6 illustrates the Mean square error curve comparison for WODGAN, DSNN, 8LCNN, DN, and VGG16 models in AD stages detection. It attests that the adversarial loss functions of the generator and discriminator $\left(L_{GAN}^{DR}=\left\|DR\left(y_{real}\right)-1\right\|_2^2+\left\|DR\left(y_{fake}\right)-0\right\|_2^2\right)$ $L_{GAN}^{GR}=\left\|DR\left(y_{fake}\right)-1\right\|_2^2$ and incorporated with the deep discriminator model in WODGAN help obtain less mean square error rate than existing classifiers.

Fig. 7 illustrates the mean absolute error curve comparison for WODGAN, DSNN, 8LCNN, DN, and VGG16 models in AD stages detection. It proves that the proper preprocessing steps such as noise removal, image enhancement, biomarker region identification and extraction, and feature reduction approaches are all incorporated with the deep discriminator model in WODGAN in obtaining less mean absolute error rate than existing classifiers.

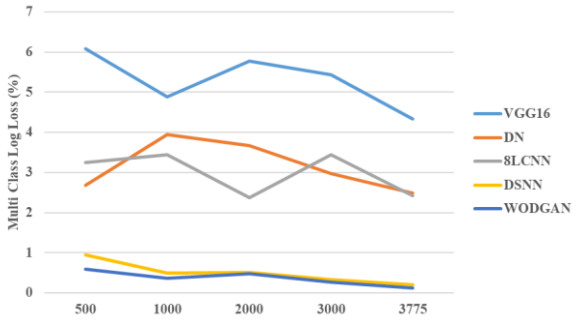

Fig. 5: Multi-class log loss value comparison

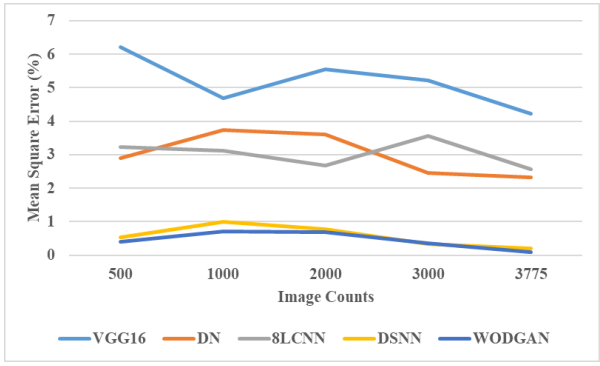

Fig. 6: Mean square error comparison

Table 4: Total performance of classifiers in ad prediction comparison

Accuracy (%)						Precision (%)						Recall (%)					
Image count	VGG 16	DN	8LC NN	DSNN	WOD GAN	Image count	VGG 16	DN	8LC NN	DSNN	WOD GAN	Image count	VGG 16	DN	8LC NN	DSN N	WOD GAN
500	93.97	97.45	96.75	99. 33	99.57	500	93.92	97.32	96.75	99. 05	99.41	500	93.78	97.11	96.76	99.46	99.60
1000	95.13	96.02	96.34	99.50	99.61	1000	95.11	96.05	96.56	99.51	99.64	1000	95.32	96.25	96.87	99.01	99.29
2000	94.09	96.92	97.32	99.45	99.56	2000	94.22	96.33	97.62	99.49	99.53	2000	94.45	96.39	97.32	99.22	99.32
3000	94.66	97.02	96.89	99.77	99.87	3000	94.56	97.02	96.55	99.66	99.74	3000	94.78	97.55	96.43	99.66	99.65
3775	95.72	97.51	97.60	99.81	99.92	3775	95.67	97.51	97.58	99. 79	99.88	3775	95.77	97.67	97.44	99.79	99.90
Mean square error (%)						Mean absolute error (%)						Multi-class log loss (%)					
500	6.08	2.68	3.25	0.95	0.59	500	6.22	2.89	3.24	0.54	0.4	500	6.03	2.55	3.25	0.67	0.43
1000	4.89	3.95	3.44	0.49	0.36	1000	4.68	3.75	3.13	0.99	0.71	1000	4.87	3.98	3.66	0.5	0.39
2000	5.78	3.67	2.38	0.51	0.47	2000	5.55	3.61	2.68	0.78	0.68	2000	5.91	3.08	2.68	0.55	0.44
3000	5.44	2.98	3.45	0.34	0.26	3000	5.22	2.45	3.57	0.34	0.35	3000	5.34	2.98	3.11	0.23	0.13
3775	4.33	2.49	2.42	0.21	0.12	3775	4.23	2.33	2.56	0.21	0.1	3775	4.28	2.49	2.4	0.23	0.08

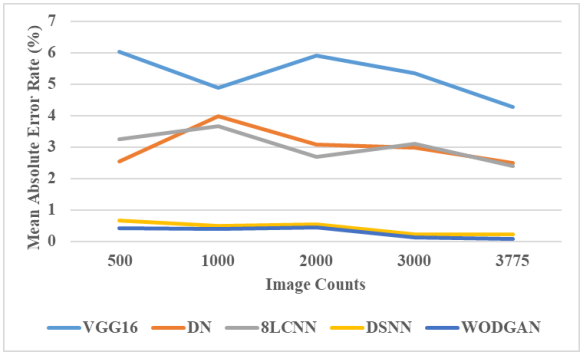

Fig. 7: Mean absolute error comparison

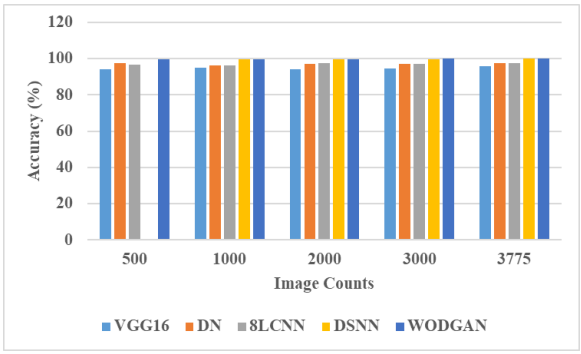

Fig. 8: Accuracy rate analysis

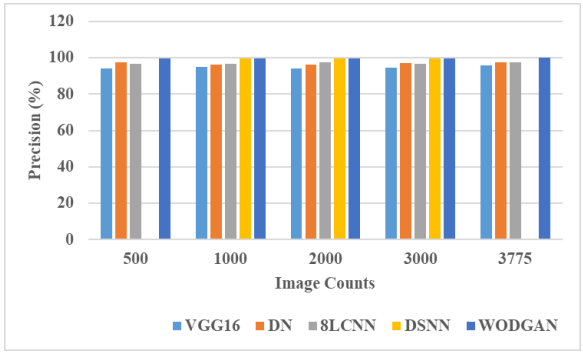

Fig. 9: Precision rate analysis

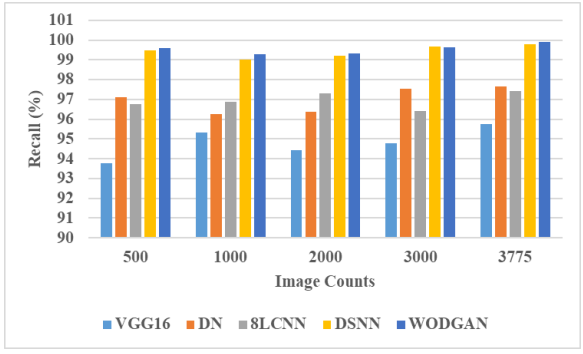

Fig. 10: Recall rate comparison

Figure 8 illustrates the accuracy rate comparison for WODGAN, DSNN, 8LCNN, DN, and VGG16 models in AD stages detection. It proves that the optimized network functionalities of the WODGAN model using the derivation of the (Eq. 26) Whale optimizer to achieve an increase in the accuracy rate of 99.92% for the WODGAN model in AD stages detection.

Figure 9 illustrates the precision rate comparison for the detection of WODGAN, DSNN, 8LCNN, DN, and VGG16 models in the AD stages. It proves that the optimized network functionalities of the WODGAN model using the derivation of (Eq. 26) Whale optimizer helps achieve a high precision rate (99.83%) than Deep comparison models.

Figure 10 illustrates the recall rate comparison for detecting WODGAN, DSNN, 8LCNN, DN, and VGG16 models in AD stages. In addition, it displays that the HSICL-based feature reduction feature $\left(HSICL: \min_{a} \frac{1}{2} \left\| L^{'} - \sum_{NN=1}^{o} a_{NN} K^{'(NN)} \right\|_{F}^{2} + \lambda \|a\| 1, a_{1.}, ..., a_{o} > 0 \right)$ incorporated in preprocessing that effectively reduces overfitting problems during model training. As a result, the model has a higher recall rate (99.90%) than comparison deep models.

The particular problematic-oriented functionalities of the WODGAN model and whale optimizers prey hunting feature in the DGAN model facilitate the optimization of the uncertainty issues and optimize the network functions effectively. These two features support attaining a high 99.92% accuracy ratio in AD stage identification. The overfitting problems are reduced by the DGAN adversarial loss functions of the generator and discriminator models as well as the HSICL-based inappropriate feature lessening function. This overfitting reduction impacts the classification model to achieve the reduced error ratio of 0.08% in AD phases recognition as compared to the other 4 comparisons Deep model methods. The section's total assessment result demonstrates that the AD detection models' features, like exact biomarker area recognition, feature enhancement, extraction, and inappropriate feature decrease methods, helped decrease overfitting during model training. The exact pathological biomarker feature identification problem and network node functionalities optimization concern has been resolved effectively with WO functionalities in DGAN.

Conclusion

Thus, the result and discussion section clearly describes the WODGAN models' performance with high and low-dimensional brain MRI images of various AD stages. In this study, the AD stages recognition system's accuracy ratio is improved maximum of 0.11% and the error ratio is reduced by up to 0.15% than existing comparison deep classifiers. Moreover, during the model training, the deep model discriminator in the DGAN model identifying the generator model generated fake MRI AD

images efficiently with WO functionalities and adversarial loss. It clearly shows that the AD detection system performs excellently, then comparing recent deep learning models. Furthermore, the feature reduction functionality incorporated WODGAN model has also reduced overfitting issues. These features help to reduce the AD misdiagnosis error issues in the existing AD detection system. It could be difficult to comprehend the precise features that influence the models' conclusions. In therapeutic situations, wherein interpretability and clarity are critical, this can reduce the trust and acceptability of the model. Researchers can use other recent deep classification models, such as the Inception network, Siamese neural network, and residual network, for future studies. Fine-tuning bio-inspired optimizer methods can also be incorporated to improve the models' performance in AD stage detection. In addition to the above the accuracy and dependability of AD stage diagnosis may be enhanced by investigating the integration of various imaging modalities, such as integrating MRI and Positron Emission Tomography (PET) imaging or additional biological markers in the future.

Acknowledgment

Thank you to the publisher for their support in the publication of this research article. We are grateful for the resources and platform provided by the publisher, which have enabled us to share our findings with a wider audience. We appreciate the efforts of the editorial team in reviewing and editing our work, and we are thankful for the opportunity to contribute to the field of research through this publication.

Funding Information

The authors received no specific funding for this study.

Author's Contributions

R. Sampath: Conception and design, acquisition of data, analysis, and interpretation of data. Drafted the article.

M. Baskar: Reviewed article critically for significant intellectual content and gave final approval of the version to be submitted and any revised version.

Ethics

This article is original and contains unpublished material. The corresponding author confirms that all of the other authors have read and approved the manuscript and that no ethical issues are involved.

Conflicts of Interest

The authors declare they have no conflicts of interest to report regarding the present study.

References

ADNI. (2017). Access data and samples. http://adni.loni.usc.edu/data-samples/access-data

AIBL Study ADNI Data. (n.d.). https://aibl.csiro.au/adni/index.html

Al-Kadi, O. S. (2017). A gabor filter texture analysis approach for histopathological brain tumor subtype discrimination. *Arxiv Preprint Arxiv*: 1704.05122. https://doi.org/10.48550/arXiv.1704.05122

Allioui, H., Sadgal, M., & Elfazziki, A. (2020). Utilization of a convolutional method for Alzheimer disease diagnosis. *Machine Vision and Applications*, *31*(4), 25. https://doi.org/10.1016/j.neuroimage.2015.01.048

Ashour, A. S., Du, C., Guo, Y., Hawas, A. R., Lai, Y., & Smarandache, F. (2019). A novel neutrosophic subsets definition for dermoscopic image segmentation. *IEEE Access*, *7*, 151047-151053. https://ieeexplore.ieee.org/abstract/document/8864984

Basaia, S., Agosta, F., Wagner, L., Canu, E., Magnani, G., Santangelo, R., & Alzheimer's disease Neuroimaging Initiative. (2019). Automated classification of Alzheimer's disease and mild cognitive impairment using a single MRI and deep neural networks. *NeuroImage: Clinical*, *21*, 101645. https://doi.org/10.1016/j.nicl.2018.101645

Beheshti, I., Demirel, H., Matsuda, H., & Alzheimer's disease Neuroimaging Initiative. (2017). Classification of Alzheimer's disease and prediction of mild cognitive impairment-to-Alzheimer's conversion from structural magnetic resource imaging using feature ranking and a genetic algorithm. *Computers in Biology and Medicine*, *83*, 109-119. https://doi.org/10.1016/j.compbiomed.2017.02.011

Brazaca, L. C., Sampaio, I., Zucolotto, V., & Janegitz, B. C. (2020). Applications of biosensors in Alzheimer's disease diagnosis. *Talanta*, *210*, 120644. https://doi.org/10.1016/j.talanta.2019.120644

Chen, Y., Jia, H., Huang, Z., & Xia, Y. (2018). Early identification of Alzheimer's disease using an ensemble of 3D convolutional neural networks and magnetic resonance imaging. *In Advances in Brain Inspired Cognitive Systems: 9th International Conference, BICS 2018, Xi'an, China, July 7-8, 2018, Proceedings 9* (pp. 303-311). Springer International Publishing. https://doi.org/10.1007/978-3-642-40763-5_72

Cheng, D., & Liu, M. (2017). Classification of Alzheimer's disease by cascaded convolutional neural networks using PET images. *In Machine Learning in Medical Imaging: 8th International Workshop, MLMI 2017, Held in Conjunction with MICCAI 2017, Quebec City, QC, Canada, September 10, 2017, Proceedings 8* (pp. 106-113). Springer International Publishing. https://doi.org/10.1007/978-3-319-67389-9_13

Damodaran, B. B., Courty, N., & Lefèvre, S. (2017). Sparse Hilbert Schmidt independence criterion and surrogate-kernel-based feature selection for hyperspectral image classification. *IEEE Transactions on Geoscience and Remote Sensing*, *55*(4), 2385-2398. https://doi.org/10.1109/TGRS.2016.2642479

Darwish, A. (2018). Bio-inspired computing: Algorithms review, deep analysis and the scope of applications. *Future Computing and Informatics Journal*, *3* (2), 231-246. https://doi.org/10.1016/j.fcij.2018.06.001

Ebrahimi-Ghahnavieh, A., Luo, S., & Chiong, R. (2019, July). Transfer learning for Alzheimer's disease detection on MRI images. *In 2019 IEEE International Conference on Industry 4.0, Artificial Intelligence and Communications Technology (IAICT)* (pp. 133-138). IEEE. https://doi.org/10.1109/ICIAICT.2019.8784845

Fan, Q., Chen, Z., Li, Z., Xia, Z., Yu, J., & Wang, D. (2021). A new improved whale optimization algorithm with joint search mechanisms for high-dimensional global optimization problems. *Engineering with Computers*, *37*, 1851-1878. https://doi.org/10.1007/s00366-019-00917-8

Feng, C., Elazab, A., Yang, P., Wang, T., Lei, B., & Xiao, X. (2018). 3D convolutional neural network and stacked bidirectional recurrent neural network for Alzheimer's disease diagnosis. *In PRedictive Intelligence in MEdicine: First International Workshop, PRIME 2018, Held in Conjunction with MICCAI 2018, Granada, Spain, September 16, 2018, Proceedings 1* (pp. 138-146). Springer International Publishing. https://doi.org/10.1007/978-3-030-00320-3_17

Garg, M., & Dhiman, G. (2021). A novel content-based image retrieval approach for classification using GLCM features and texture fused LBP variants. *Neural Computing and Applications*, *33*, 1311-1328. https://doi.org/10.1007/s00521-020-05017-z

Gupta, B., & Verma, A. R. (2020). A novel approach of 2D adaptive filter based on MPSO technique for biomedical image. *Augmented Human Research*, *5*(1), 1. https://doi.org/10.1007/s41133-019-0017-2

Haq, A. U., Li, J. P., Memon, M. H., Nazir, S., & Sun, R. (2018). A hybrid intelligent system framework for the prediction of heart disease using machine learning algorithms. *Mobile Information Systems*, 2018, 1-21. https://doi.org/10.1155/2018/3860146

Jain, R., Jain, N., Aggarwal, A., & Hemanth, D. J. (2019). Convolutional neural network-based Alzheimer's disease classification from magnetic resonance brain images. *Cognitive Systems Research*, *57*, 147-159. https://doi.org/10.1016/j.cogsys.2018.12.015

Jha, D., & Kwon, G. (2017). Alzheimer's disease detection using sparse autoencoder, scale conjugate gradient and softmax output layer with fine tuning. *International Journal of Machine Learning and Computing*, *7*(1), 13-17. https://doi.org/10.18178/ijmlc.2017.7.1.612

Kazemi, Y., & Houghten, S. (2018, May). A deep learning pipeline to classify different stages of Alzheimer's disease from fMRI data. *In 2018 IEEE Conference on Computational Intelligence in Bioinformatics and Computational Biology (CIBCB)* (pp. 1-8). IEEE. https://doi.org/10.1109/CIBCB.2018.8404980

Leandrou, S., Petroudi, S., Kyriacou, P. A., Reyes-Aldasoro, C. C., & Pattichis, C. S. (2018). Quantitative MRI brain studies in mild cognitive impairment and Alzheimer's disease: A methodological review. *Ieee Reviews in Biomedical Engineering*, *11*, 97-111. https://doi.org/10.1109/RBME.2018.2796598

Li, W., Lin, X., & Chen, X. (2020). Detecting Alzheimer's disease Based on 4D fMRI: An exploration under deep learning framework. *Neurocomputing*, *388*, 280-287. https://doi.org/10.1016/j.neucom.2020.01.053

Lian, C., Liu, M., Zhang, J., & Shen, D. (2018). Hierarchical fully convolutional network for joint atrophy localization and Alzheimer's disease diagnosis using structural MRI. *IEEE Transactions on Pattern Analysis and Machine Intelligence*, *42*(4), 880-893. https://doi.org/10.1109/TPAMI.2018.2889096

Liu, M., Li, F., Yan, H., Wang, K., Ma, Y., Shen, L., & Alzheimer's disease Neuroimaging Initiative. (2020). A multi-model deep convolutional neural network for automatic hippocampus segmentation and classification in Alzheimer's disease. *Neuroimage*, *208*, 116459. https://doi.org/10.1016/j.neuroimage.2019.116459

Lucas, F., Costa, P., Batalha, R., Leite, D., & Škrjanc, I. (2020). Fault detection in smart grids with time-varying distributed generation using wavelet energy and evolving neural networks. *Evolving Systems*, *11*, 165-180. https://doi.org/10.1007/s12530-020-09328-3

Lu, D., Popuri, K., Ding, G. W., Balachandar, R., & Beg, M. F. (2018). Multimodal and multiscale deep neural networks for the early diagnosis of Alzheimer's disease using structural MR and FDG-PET images. S*cientific Reports*, *8*(1), 5697. https://doi.org/10.1038/s41598-018-22871-z

Marcus, D. S., Wang, T. H., Parker, J., Csernansky, J. G., Morris, J. C., & Buckner, R. L. (2007). Open Access Series of Imaging Studies (OASIS): Cross-sectional MRI data in young, middle aged, nondemented, and demented older adults. *Journal of cognitive Neuroscience*, *19*(9), 1498-1507. https://doi.org/10.1162/jocn.2007.19.9.1498

Nawaz, H., Maqsood, M., Afzal, S., Aadil, F., Mehmood, I., & Rho, S. (2021). A deep feature-based real-time system for Alzheimer disease stage detection. *Multimedia Tools and Applications*, *80*, 35789-35807. https://doi.org/10.1007/s11042-020-09087-y

NITRC: MIRIAD (Minimal Interval Resonance Imaging in Alzheimer's Disease): Tool/resource info. (n.d.). From Nitrc.org website: https://www.nitrc.org/projects/miriad/

Niu, J., & Tang, X. (2020, October). 3D residual dense convolutional network for diagnosis of Alzheimer's disease and mild cognitive impairment. I*n 2020 IEEE International Conference on Mechatronics and Automation (ICMA)* (pp. 1581-1586). IEEE. https://doi.org/10.1109/ICMA49215.2020.9233674

Ortiz, A., Munilla, J., Martínez-Murcia, F. J., Górriz, J. M., Ramírez, J., & Alzheimer's disease Neuroimaging Initiative. (2017). Learning longitudinal MRI patterns by SICE and deep learning: Assessing the Alzheimer's disease progression. *In Medical Image Understanding and Analysis: 21st Annual Conference, MIUA 2017, Edinburgh, UK, July 11–13, 2017, Proceedings 21* (pp. 413-424). https://doi.org/10.1007/978-3-319-60964-5_36

Saxena, D., & Cao, J. (2019). D-GAN: Deep generative adversarial nets for spatio-temporal prediction. *Arxiv Preprint Arxiv*: 1907.08556. https://doi.org/10.48550/arXiv.1907.08556

Shi, B., Chen, Y., Zhang, P., Smith, C. D., Liu, J., & Alzheimer's disease Neuroimaging Initiative. (2017a). Nonlinear feature transformation and deep fusion for Alzheimer's disease staging analysis. *Pattern Recognition*, *63*, 487-498. https://doi.org/10.1016/j.patcog.2016.09.032

Shi, J., Zheng, X., Li, Y., Zhang, Q., & Ying, S. (2017b). Multimodal neuroimaging feature learning with multimodal stacked deep polynomial networks for diagnosis of Alzheimer's disease. IEEE *Journal of Biomedical and Health Informatics*, *22*(1), 173-183. https://doi.org/10.1109/JBHI.2017.2655720

Singh, P., Mukundan, R., & De Ryke, R. (2020). Feature enhancement in medical ultrasound videos using contrast-limited adaptive histogram equalization. *Journal of Digital Imaging*, *33*, 273-285. https://doi.org/10.1007/s10278-019-00211-5

Vu, T. D., Ho, N. H., Yang, H. J., Kim, J., & Song, H. C. (2018). Non-white matter tissue extraction and deep convolutional neural network for Alzheimer's disease detection. *Soft Computing*, *22*, 6825-6833. https://doi.org/10.1007/s00500-018-3421-5

Wang, H., Shen, Y., Wang, S., Xiao, T., Deng, L., Wang, X., & Zhao, X. (2019). Ensemble of 3D densely connected convolutional network for diagnosis of mild cognitive impairment and Alzheimer's disease. *Neurocomputing*, *333*, 145-156. https://doi.org/10.1016/j.neucom.2018.12.018

Wang, S. H., Phillips, P., Sui, Y., Liu, B., Yang, M., & Cheng, H. (2018). Classification of Alzheimer's disease based on eight-layer convolutional neural network with leaky rectified linear unit and max pooling. *Journal of Medical Systems*, *42*, 1-11. https://doi.org/10.1007/s10916-018-0932-7

Wee, C. Y., Liu, C., Lee, A., Poh, J. S., Ji, H., Qiu, A., & Alzheimers Disease Neuroimage Initiative. (2019). Cortical graph neural network for AD and MCI diagnosis and transfer learning across populations. *NeuroImage: Clinical*, *23*, 101929. https://doi.org/10.1016/j.nicl.2019.101929